A Static-Sample Magnetometer for Characterizing Weak Magnetic Materials

A Static-Sample Magnetometer for Characterizing Weak Magnetic Materials

Pasquale Arpaia, *Senior Member, IEEE*, Marco Buzio, Alessandro Parrella, Mariano Pentella, *Student Member, IEEE*, and Pedro M. Ramos, *Senior Member, IEEE*

***Abstract*— In this article, a static-sample magnetometer is presented to measure the relative permeability of weakly magnetic materials. The method consists of scanning the magnetic field inside a dipole magnet by using an NMR teslameter to measure the perturbation of a test specimen on the externally applied field. Then, an inverse problem is used to compute the specimen's relative permeability. As a case study, the measurement of three different materials with different shapes and dimensions is carried out. The method was validated by measuring the same material by vibrating sample magnetometry as proposed by the standard ASTM A342/A342M-14. The expanded measurement uncertainty of the relative permeability, evaluated by Monte Carlo simulations, is about 10^{-4} for all the cases, with a level of confidence of 95%.**

***Index Terms*— Inverse problem approach, magnetic measurements, NMR teslameter, relative permeability, stainless steel, tungsten, vibrating sample magnetometer, weak magnetic materials.**

I. Introduction

IN ALLOYS such as austenitic stainless steels, brass, and bronze, weak traces of martensite are present [1]. Among pure metals, aluminum is the reference for these kinds of applications, though its mechanical properties are often inadequate for specific tasks or applications. Titanium is a valid alternative, but its high cost makes it only usable for specific applications (e.g., vacuum chambers). Finally, as an alternative to metals, ceramics have lower susceptibility, but they are often too brittle to be employed instead of metals. A good compromise among all these requirements is stainless steel. In particular, austenitic stainless steels are broadly used in harsh environments, such as nuclear reactors, naval vessels, and chemical plants, where the combination of good corrosion resistance with suitable mechanical properties is crucial. Stainless steel is also often used in cryogenics, mainly for their low magnetic permeability and its minimal variation during a cooling down process [1]. Zirconium alloys, or zircaloys, are another important category. In particular, they are employed in nuclear applications because of their good corrosion resistance and low neutron absorptions rates [2]. Moreover, they are biocompatible and used in orthopedic and dental implants where their low susceptibility plays a crucial role to guarantee compatibility with magnetic resonance imaging (MRI) machines [3].

Independently of the application, weakly magnetic materials require quality control of their magnetic properties. In the vast available literature, several methods are proposed. The standard ASTM A342/A342M-14 "Standard Test Methods for Permeability of Weakly Magnetic Materials" [4] describes four different approaches. The first one is the flux-metric method performed on open-circuit samples, where the demagnetizing field leads to an underestimation of the relative permeability. A solution employing closed-circuit samples was proposed in the literature [5], but the poor signal-to-noise ratio leads to an uncertainty of more than 5% and a lower bound of measurable permeability of 1.001. The second standard method is the approach via low-μ permeability indicators, portable instruments based on the comparison of the permeability of the test specimen with a standard insert having known permeability. The drawback is that the maximum excitation magnetic field is limited (i.e., 8 kA/m [6]), whereas fields higher than 100 kA/m are recommended, due to the variability of the permeability with the applied field. The third standard method is the flux distortion method, used for portable instruments as well [7], but they present limitations in accuracy (5%) and the sample shape must be only cylindrical. The fourth standard method is the vibrating sample magnetometry (VSM) [8]. The technique consists in magnetizing the sample in a uniform and constant magnetic field H_{ext}. Afterward, the specimen is sinusoidally vibrated using a linear motor. This vibration determines flux variations that are detected by a sensing coil and proportional to the magnetic moment m of the specimen under test. The permeability is then calculated from the magnetic moment as $\mu_r = (m/V + H_{\text{ext}})/H_{\text{ext}}$, where V is the volume of the speci-

Manuscript received January 17, 2020; revised November 10, 2020; accepted November 21, 2020. Date of publication December 2, 2020; date of current version December 31, 2020. This work was supported in part by Fundação para a Ciência e a Tecnologia (FCT) − Ministério da Ciência, Tecnologia e Ensino Superior (MCTES) under Project UIDB/EEA/50008/2020. The Associate Editor coordinating the review process was Branislav Djokic. *(Corresponding author: Pasquale Arpaia.)*

Pasquale Arpaia is with the Department of Electrical Engineering and Information Technology, University of Naples Federico II, 80138 Naples, Italy (e-mail: pasquale.arpaia@unina.it).

Marco Buzio and Alessandro Parrella are with the Magnets, Superconductors and Cryostat Group, Technology Department, European Organization for Nuclear Research (CERN), 1211 Geneva, Switzerland (e-mail: marco.buzio@cern.ch; alessandro.parrella@cern.ch).

Mariano Pentella is with the Department of Applied Science and Technology, Politecnico di Torino, 10129 Turin, Italy, and also with the Magnets, Superconductors and Cryostat Group, Technology Department, European Organization for Nuclear Research (CERN), 1211 Geneva, Switzerland (e-mail: mariano.pentella@cern.ch).

Pedro M. Ramos is with the Instituto Superior Técnico, University of Lisbon, 1649-004 Lisbon, Portugal, and also with the Instituto de Telecomunicações, University of Lisbon, 1649-004 Lisbon, Portugal (e-mail: pedro.m.ramos@tecnico.ulisboa.pt).

Digital Object Identifier 10.1109/TIM.2020.3041823

men. This method is considered as the reference to test weakly magnetic materials due to its high accuracy (10^{-5} on the relative permeability) and the broad range of test temperatures. Nonetheless, its use is limited to specialized laboratories due to the cost and expertise know-how required. Another alternative technique is the superconducting quantum interference device (SQUID) magnetometry [9]. Although the performance is comparable with the VSM [10], the SQUID magnetometer has high costs and requires expertise know-how for operation. The same problems also affect the alternating-gradient force magnetometer (AGFM) [11], a method based on detecting the force on the specimen due to the application of a field gradient. Finally, there are DC susceptometers, generally used for the microscopic characterization of weakly magnetic materials [12]. Recent trends in the state of the art show the increasing application of inverse problem techniques to solve a broad variety of problems [13]–[18], including the characterization of magnetic materials employed in electromagnetic devices such as electrical machines [19], magneto-rheological elastomers [20], or circuit breakers [21]. Although there are a broad variety of solutions, the characterization of weakly magnetic materials by using the inverse problem approach has not been previously considered.

In this article, a static-sample magnetometer (SSM) to characterize weakly magnetic materials is presented. The measurement system is based on an approach initially proposed in [22], which combines a flux distortion method and an inverse problem approach, and the method validation was performed on cylindrical reference samples. The work presented in this article improves the performances of this method, which was extended to samples with any shape and dimensions. The characterization of three different materials for a total of six different test specimens having different shapes and dimensions is presented. The uncertainty of the measurement method was assessed by the Monte Carlo analysis and the results are compared with a VSM.

II. Experimental Method

A. Static-Sample Magnetometry

The static-sample magnetometry consists of inserting the specimen to be tested inside a dipolar and highly uniform magnetic field to measure how the sample perturbs it. The relative permeability of the test specimen is then calculated by setting up an optimization problem. The test bench setup is shown in Fig. 1.

The field, generated by the magnet coils, is scanned twice in the midplane of the magnet gap by using an NMR teslameter moved by a linear motor: to map the background field without the sample and, then, to scan the field in the presence of the sample. A second fixed NMR teslameter is used as a reference to monitor undesired perturbations due to oscillations in the excitation current of the magnet. The use of NMR probes is crucial to detect the field perturbation created by the specimen, typically in the order of 100 μT. Other systems, largely used in magnetic measurements, such as coils and Hall probes, present poor accuracy for this kind of application (roughly 100 μT).

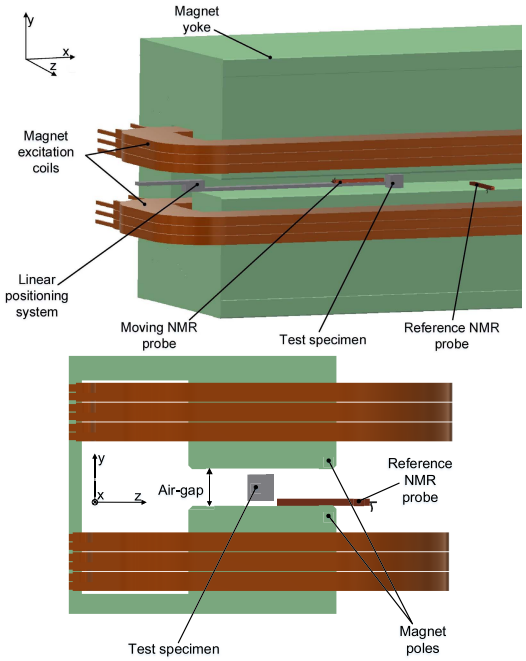

Fig. 1. Top: layout of the test bench. Bottom: detail of the magnet gap.

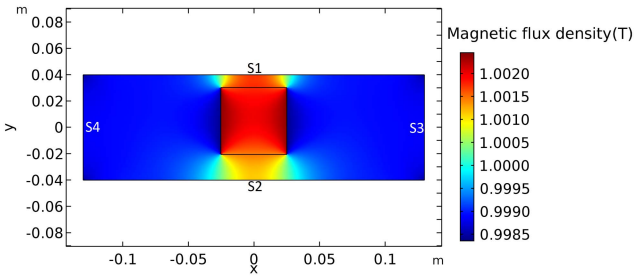

Fig. 2. Example of FE results for the optimization problem. S_1 and S_2 are upper and lower bounds, whereas S_3 and S_4 are the right- and left-hand boundaries, respectively.

Coils can also reach 1 μT of accuracy with proper calibration techniques, but they would require a more complex layout.

The measured values of the background field are provided as input to a 3-D finite element (FE) model. Fig. 2 shows an example of a 3-D simulation. If the sample has an axisymmetric geometry, a 2-D axisymmetric model is adopted to reduce the simulation time.

The simulation is performed by adopting the magnetostatic model in terms of reduced magnetic scalar potential formulation [23]. The total magnetic field $\mathbf{H}$ is therefore defined as

$$\mathbf{H} = \mathbf{H}_b - \nabla \psi_p \tag{1}$$

where $\mathbf{H}_b$ is assessed from the measured background field $\mathbf{B}_b$ as $\mathbf{H}_b = \mathbf{B}_b/\mu_0$, with μ_0 the permeability of the free space. ψ_p is the reduced magnetic scalar potential. From Maxwell's equations, the total magnetic flux density $\mathbf{B}$ must be divergence-free. Hence, with $\mathbf{B} = \mu_r \mu_0 \mathbf{H}$, this yields

$$\begin{cases} \nabla \cdot [\mu_r \mu_0 (-\nabla \psi_p + \mathbf{H}_b)] = 0 \\ \psi_p = 0|_{S_1} \\ \psi_p = 0|_{S_2} \\ \nabla \psi_p \cdot \mathbf{n} = 0|_{S_3, S_4} \end{cases} \tag{2}$$

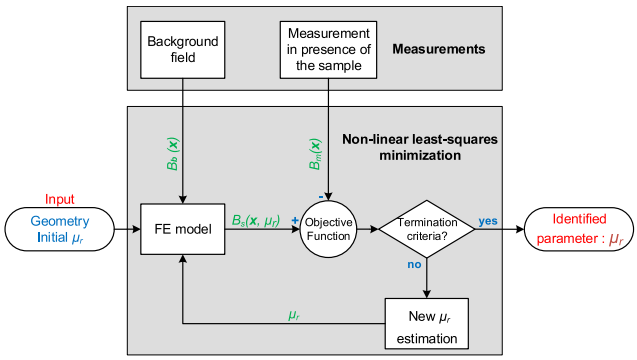

Fig. 3. Flowchart of the optimization problem.

where μ_r is the relative magnetic permeability assumed to be uniform within the specimen, S_1 and S_2 are the upper and the lower boundaries of the domain, respectively, S_3 and S_4 are the right and left side boundaries, respectively, $\mathbf{n}$ is the normal vector to the boundaries S_3 and S_4. If the geometry of the specimen is axisymmetric, the specimen is placed with its axis perpendicular to the poles. The measured background field has only the y-component and depends only on the x-coordinate, and therefore, $\mathbf{B}_b = B_b(x)\ \mathbf{e}_y$, with $\mathbf{e}_y$ unit vector parallel to the y-axis. The probe (y, z)-coordinates are known and are measured separately.

The optimization problem consists of finding the relative permeability μ_r that minimizes the cost function

$$f(\mu_r) = \sum_{k=1}^{N} |B_m(x_k) - B_s(\mu_r, x_k)|^2 \tag{3}$$

where B_m is the magnetic field measured in the presence of the sample and B_s is the FE simulated field and x_k are the discrete x-coordinates of the N points where the field is measured. The optimization is performed by the Levenberg–Marquardt algorithm [24], [25] in a MATLAB[1] environment, while the FE analysis is carried out in COMSOL.[1] The optimization procedure is summarized in the flowchart presented in Fig. 3.

The termination criteria of the optimization procedure are: $\sqrt{f} \leq 10\ \mu$T or minimum step size $\Delta\mu_r \leq 10^{-6}$. The method does not critically depend on the initial guess. Therefore, a relative permeability value of 1, close to typical values for weakly magnetic materials, can be used for the initial value. If the material typical permeability is known, it can be used to increase the rate of convergence of the optimization.

B. Uncertainty Sources

In this section, the uncertainty sources are outlined. The sources, summarized in Fig. 4, can be divided into the following: 1) measurement uncertainties and 2) modeling uncertainties.

The measurement uncertainties arise from the field measurements, the probe positioning, and the dimensions and positioning of the sample.

The field measurement uncertainty is given by the NMR teslameter, necessary to measure the field with very high accuracy (5 ppm) and resolution (0.1 μT). The measured field is considered as the only function of the spatial coordinate x. The field variations along the y- and z-coordinates lie within the accuracy range of the NMR teslameter, and therefore, they are neglected.

The probe positioning uncertainty is the uncertainty on the coordinates (x, y) where the field is measured. The x-coordinate uncertainty depends on the accuracy of the linear motor (10 μm). The y-coordinate uncertainty is due to the uncertainty on the probe distance from the pole. Both x and y-coordinates include the contribution of the positioning uncertainty of the active element within the NMR probe, known from the datasheet.

The modeling uncertainty sources depend on the accuracy of the FE model used to fit the measurements. The accuracy of the model described by (2) depends on: 1) geometrical uncertainties and 2) neglecting the background field variations. The geometrical uncertainties arise from the domain geometry used for the simulation. The length of the domain is equal to the distance along which the field is scanned. Hence, its uncertainty is the same as the linear motor. The height and the depth of the domain are, respectively, equal to the air-gap length and the width of the pole, known within a specific tolerance value (10^{-4} m).

Background field variations originate from different concurring causes. The main one is the air-reluctance variation due to the sample insertion. This arises from the presence of the magnet yoke, made of a ferromagnetic material, not considered in the simulation, which is performed only in the air-gap region. This effect can be easily measured at the maximum distance from the sample, where the perturbations should be ideally zero. At a distance of more than twice the scan length, this effect completely disappears, and therefore, it cannot be detected by the reference NMR. This assumption results in a deterministic effect that would lead to an overestimation of the relative permeability and a poor fit quality. This systematic contribution depends on the permeability and the dimensions of the specimen under test and, thus, it is not known *a priori*. Other minor contributions concurring to variations of the background field are due to the low-frequency current variations deriving from the power converter instabilities and leading to field variations in the order of 1 ppm. These are linearly compensated by using the reference NMR measurements. The total background field variation is considered by introducing a constant term correction in the optimization problem with initial value

$$\Delta B_b = B_b(\Delta x_{\max}) - B_m(\Delta x_{\max}). \tag{4}$$

This choice for the initial value derives from the fact that ΔB_b should be ideally zero. Therefore, the modified cost function is

$$f(\mu_r, \Delta B_b) = \sum_{k=1}^{N} |B_m(x_k) - B_s(\mu_r, \Delta B_b, x_k)|^2. \tag{5}$$

III. Results and Discussion

A. Sample Preparation

The case study consists of the magnetic characterization of six different test specimens, shown in Fig. 5: two made

[1]Registered trademark.

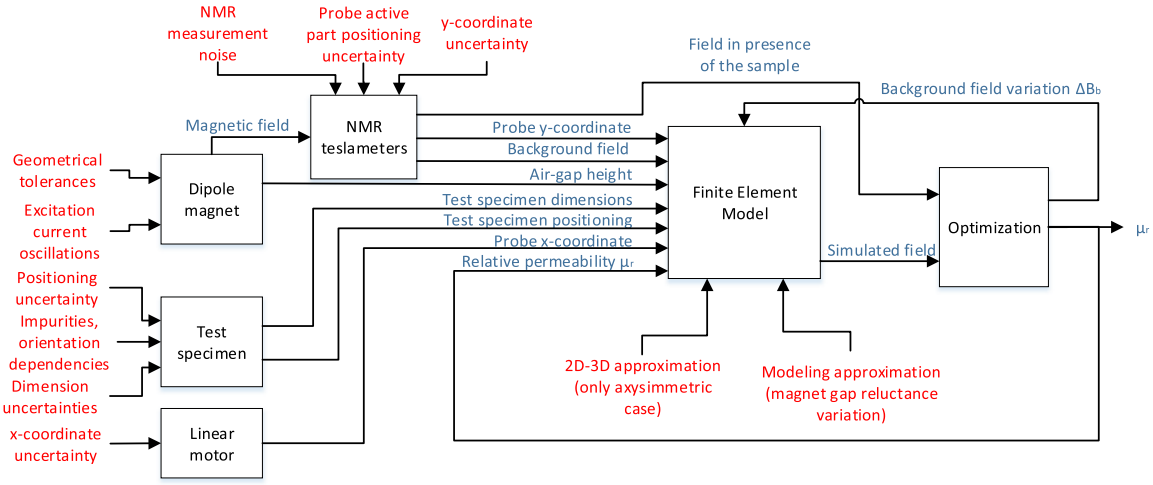

Fig. 4. Summary of the uncertainty sources. Blue: measurement parameters with their uncertainty. Red: uncertainty sources.

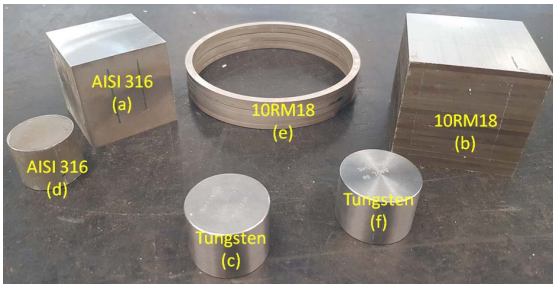

Fig. 5. Test specimens measured by static-sample magnetometry. (a) AISI 316, cube; (b) 10RM18, laminations; (c) Tungsten 1, cylinder; (d) AISI 316, cylinder; (e) 10RM18, toroids; (f) Tungsten 2, cylinder.

of AISI 316 stainless steel, two made of tungsten, and two made of 10RM18, which is another stainless steel alloy. The test specimens have different shapes and dimensions. The two AISI 316 samples are a cube with 50 mm side and a cylinder with 30 mm diameter and 25 mm height. Both were cut from a single cylindrical block of steel by electrical discharge machining (EDM). The two 10RM18 specimens are a stack of square laminations, forming a cube with 60 mm side, and a stack of toroids with 114 mm external diameter, 105 mm internal diameter, and 18 mm total height. Both were cut from two slabs by EDM. The two tungsten specimens are cylinders with 35 mm diameter and 25 mm height.

B. Measurement Results

Fig. 1 shows the measurement system layout. Two NMR teslameters Metrolab PT2025 [26] and a linear positioning system PI M-511.DG [27] were used to perform the measurements. The active element is known to be at 6 ± 0.5 mm of distance from the probe edges. A Keithley 2700/7700/E Digital Multimeter [28] was used to monitor the magnet current, and a Leica Absolute Tracker AT930 [29] was used for the alignment of the stage. A dipole magnet generates a background field ranging from 0.4 to 1 T with a maximum spatial peak-to-peak oscillation of 1 mT. The magnet air gap is 80 mm, the pole width is 210 mm, and the magnet length is 2.5 m.

Fig. 6 shows the measured and the FE simulated field for the six samples. The latter was evaluated by using the relative permeability, resulting from the inverse problem, at a nominal field of 1 T. The distance between simulations and measurements is expressed in terms of root mean square error, ϵ

$$\epsilon = \sqrt{\frac{1}{N}\sum_{k=1}^{N}[B_m(x_k) - B_s(x_k)]^2}. \tag{6}$$

In the presence of the sample, the field has the same non-monotonic profile in four over six cases. For the two tungsten samples, the field has the same profile as the background field, but it has a lower initial value (of 10 μT). This is due to the low permeability. For all the samples, at a certain distance, the perturbation becomes negligible. However, a small field offset (4 μT in the worst case, AISI 316 cube) may be visible due to the background field variation described in Section II-B.

The analysis on different specimens having different shapes and permeabilities highlights how the perturbed field changes. In particular, for two samples of the same material, the perturbed field has a similar initial value, but the perturbation decays on a shorter distance for a smaller specimen size. This determines a higher slope in the initial region of the field scan. On the other hand, for similar-sized specimens of different materials, the higher is the material permeability, the larger is the difference between background and perturbed field.

The tungsten samples highlight the limits of the proposed method, as the perturbed field does not change significantly with respect to the background field. The root-mean-square error ranges from 0.4 to 1 μT. This indicates good performance in terms of fit quality, in comparison to the standard uncertainty of the measured field for each point ($\approx$3 ppm, corresponding to $\approx$3 μT at 1 T). The measurement method was validated by testing samples with different sizes of the same three materials, in a different accredited laboratory, according to the ASTM A342/A342M-14 standard by VSM performed with an MPMS-XL5 magnetometer from Quantum Design. Fig. 7 shows the measured permeabilities as a function of the nominal background field. The reported values are averages of multiple measurements.

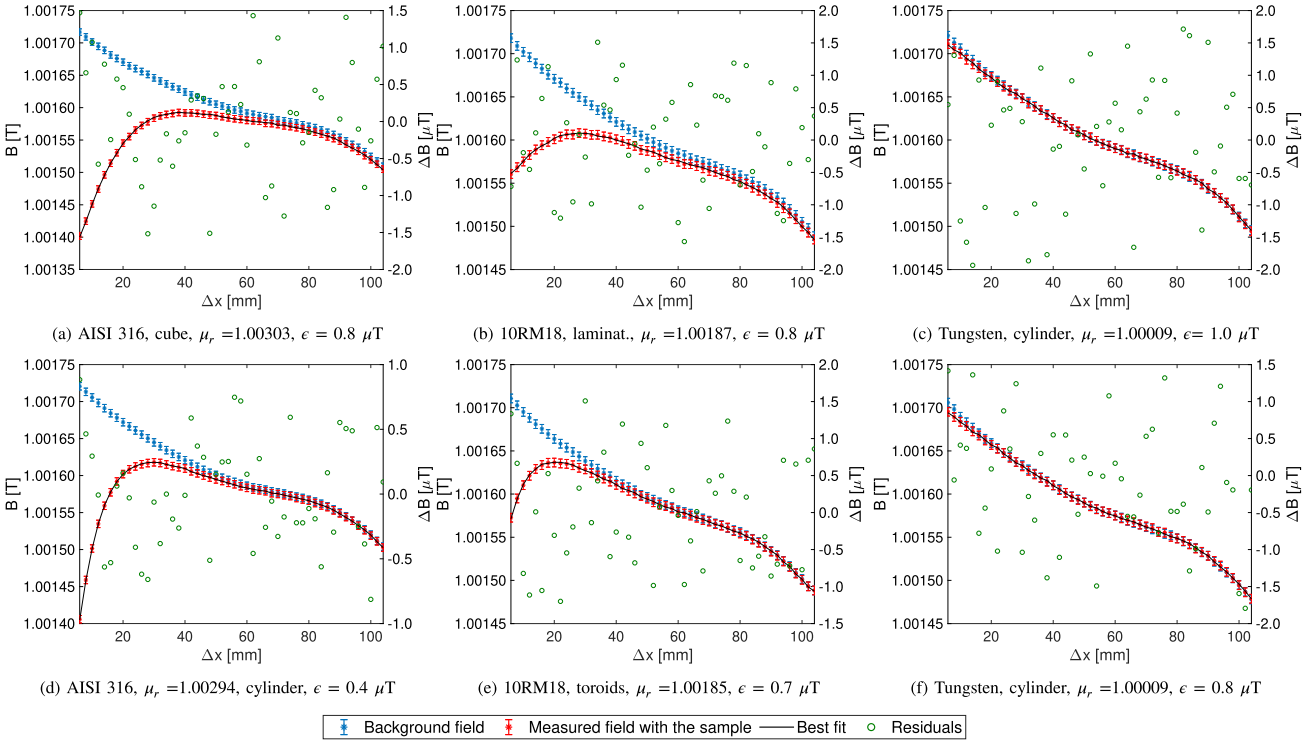

Fig. 6. Magnetic field in the presence of the specimens as a function of the distance from the sample Δx (red curve). Black curve: simulated field. Blue curve: measured background field. Green points: residuals, displayed on the right vertical axes.

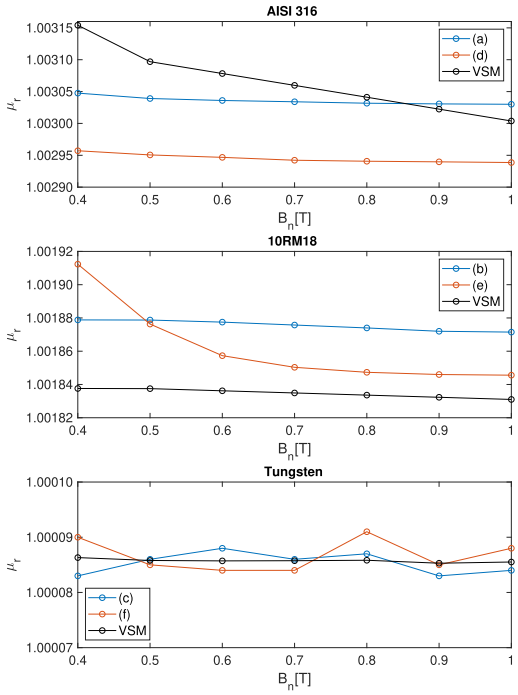

Fig. 7. Relative permeability values as a function of the nominal background field B_n. Black line: VSM measurements shown for comparison.

The measured values are all closely comparable with the references. For the tungsten samples, deviations with respect to the average values are below 10^{-5} and thus not significant. Only for the 10RM18 toroids, the permeability values increase significantly. This could be due to the machining of the specimen. As reported in the literature [30], some techniques to machine the sample may leave traces of surface impurities (principally oxides and carbon) and cause the formation of delta ferrite, a ferromagnetic phase [12]. This determines an increase in the permeability dependent on the surface-to-volume ratio of the specimen. The presence of a ferromagnetic-like behavior, although not significant, can be observed also for samples (a), (d), and (b) at lower field values.

C. Uncertainty Evaluation

The uncertainty assessment was performed by the Monte Carlo method, according to the standard ISO/IEC Guide 98-3:2008 [31] and its supplement 1 [32]. Table I summarizes the distributions assigned to each model input. The standard uncertainty values for each source of uncertainty were retrieved from the datasheets of the instruments by using the approach mentioned in [31].

Fig. 8 shows the results for each test specimen, evaluated at a nominal field of 1 T, obtained by running 3000 simulations. Each figure shows the average value and the coverage interval corresponding to a 95% of level of confidence. The values are reported in Table II. Fig. 9 shows their comparison with the measurements performed by VSM.

The measurement performed on different specimens of the same material is compatible with their respective reference measurements. Moreover, all the distributions resulting from the Monte Carlo simulations, except for the tungsten cases, are

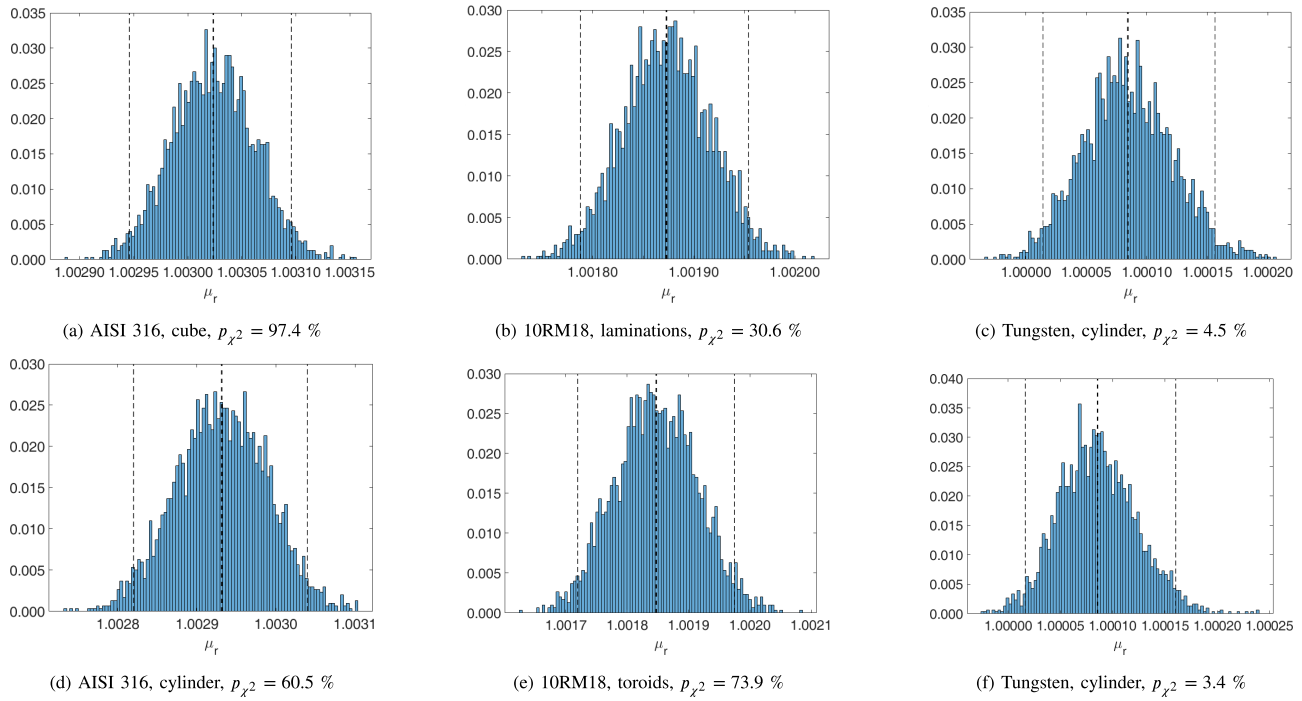

(a) AISI 316, cube, $p_{\chi^2} = 97.4$ %

(b) 10RM18, laminations, $p_{\chi^2} = 30.6$ %

(c) Tungsten, cylinder, $p_{\chi^2} = 4.5$ %

(d) AISI 316, cylinder, $p_{\chi^2} = 60.5$ %

(e) 10RM18, toroids, $p_{\chi^2} = 73.9$ %

(f) Tungsten, cylinder, $p_{\chi^2} = 3.4$ %

Fig. 8. Results of the Monte Carlo simulation for the six cases, corresponding to the curves shown in Fig. 6. The thick dashed line is the average value. The two thin dashed lines represent an interval with 95% level of confidence.

TABLE I

DISTRIBUTION ASSIGNED TO EACH MEASURED VALUE

Source of Uncertainty	Probability Distribution	Standard Uncertainty
Field measurements	Uniform	$5/\sqrt{3}$ ppm
Sample dimensions	Uniform	$10/\sqrt{3}$ μm
Domain dimensions	Uniform	$100/\sqrt{3}$ μm
y-coordinate of the probe	Uniform	$10/\sqrt{3}$ μm
x and y-coordinate of the NMR active element	Uniform	$500/\sqrt{3}$ μm
Sample distance from the lower pole	Uniform	$10/\sqrt{3}$ μm

TABLE II

MONTE CARLO SIMULATION RESULTS FOR THE ESTIMATION OF THE RELATIVE PERMEABILITY AND THE INTERVALS FOR A 95% OF LEVEL OF CONFIDENCE

Sample	Average value	Standard deviation	Coverage interval (95 %)
(a) AISI 316 (Cube)	1.003024	0.000038	[1.002948 1.003096]
(d) AISI 316 (Cyl.)	1.002932	0.000057	[1.002818 1.003041]
(b) 10RM18 (Lam.)	1.001873	0.000043	[1.001788 1.001952]
(e) 10RM18 (Tor.)	1.001847	0.000067	[1.001719 1.001975]
(c) Tungsten (Cyl.)	1.000084	0.000037	[1.000014 1.000156]
(f) Tungsten (Cyl.)	1.000085	0.000037	[1.000016 1.000160]

approximately Gaussian. This results from the chi-squared test at a 5% significance level. The p-values are reported in Fig. 8. The two tungsten distributions are close to a Gaussian distribution, but they present some skewness. This asymmetry may be explained by a permeability value extremely close to 1 that represents a limit value. In fact, according to the experimental data, $B_m \leq B_b$: this implies that $\mu_r \geq 1$. If this is not verified, the specimen would be diamagnetic. The higher uncertainty values are in correspondence of the smallest specimens, due to the higher influence of the air paramagnetic behavior and the higher sensitivity to the probe positions. Among the three materials, the only case where this seems to not happen is the tungsten case. However, by comparing the standard deviations with $(\mu_r - 1)$, the standard deviation is 44%, one order of magnitude higher than the toroids (about 4%) and the AISI 316 cylinder (2%). Moreover, by comparing the standard deviations of the AISI 316 cube (1.3%) and the 10RM18 laminations (2.14%) that have comparable dimensions, the conclusion is that the relative uncertainty decreases as the permeability increases. Although the two tungsten cases are the ones with the highest relative uncertainty, their values are the closest to their corresponding reference measurements. As reported in Section III-B, this might be explained by the fact that the sample preparation had a negligible effect on the material properties, in contrast with the two stainless steel cases. However, this indicates that the standard uncertainty has been overestimated. In detail, among the sources reported in Table I, the probe position is the most significant source of uncertainty and it mostly depends on the position of the active element within the probe. The position of the active element within the probe is known with an accuracy of 0.5 mm from the datasheet because of its inaccessibility. The sensitivity

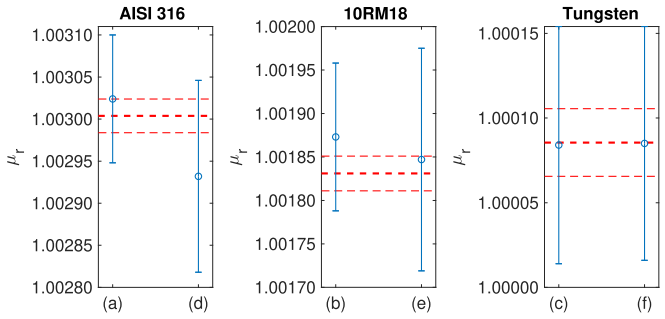

Fig. 9. Comparison of the measurement results at a nominal field of 1 T. Blue line: values and the coverage intervals resulting from the Monte Carlo simulations. The thick red dashed line is the reference value measured by VSM, whereas the thin dashed red lines are the coverage interval corresponding to a 95% of level of confidence.

coefficient of the probe coordinates ranges between 0.012 and 0.084 m^{-2} depending on the sample dimensions. This position should be set with better precision to improve the standard uncertainty of the results. The other two most significant sources of uncertainty are the field measurement and the domain dimensions (mainly the air-gap length).

The reported values of the standard deviations and coverage intervals have to be intended, solely, as model-related uncertainties. One should consider extra contributions, such as not-modeled parameters. For instance, for the 3-D model, the description can be considered as exhaustive, if the scan is performed as closer as possible to the midplane of the magnet gap; for the 2-D axisymmetric model, an eventual systematic error, resulting from a misalignment of the cylinder radius with the magnet x-axis, is not considered. Such contributions may produce a nonnegligible underestimation of the permeability (about 10^{-4} for the AISI 316 specimen and about 2×10^{-4} for the tungsten). To avoid this, care should be taken in placing the specimen within the air gap of the magnet.

Finally, the last contributions to be considered are sample orientation dependencies and material impurities. The sample orientation dependencies have been verified by repeating the measurement three times for each x-, y-, and z-axis [i.e., [1.00303, 1.00302, 1.00303] for the specimen (a)]. Sample impurities need separate measurements because no particular assumptions can be done on their distribution. The approach used in this article was to produce different specimens from the main material slab and assess how much they differ in terms of permeability. This has led to differences of 10^{-5} for the tungsten, 5×10^{-5} for the AISI 316, and 2×10^{-5} for the 10RM18 alloy.

IV. Conclusion

In this article, an SSM to test weakly magnetic materials was presented. The method consisted of scanning the magnetic field inside a dipole magnet by using an NMR teslameter to measure the perturbation of a test specimen on the externally applied field. Then, an inverse problem combined with FE analysis was set up to retrieve the magnetic permeability of the material.

The method was validated by using as reference the VSM, as reported in the standard ASTM A342/A342M-14.

The uncertainty was assessed by performing a Monte Carlo analysis. The results showed that all the measurements are compatible with the reference within an uncertainty of the order of 10^{-4}.

The main advantage of the proposed method is the high accuracy despite the simple but expensive measurement layout, provided the availability of a dipole magnet capable of delivering a uniform field, often the case in magnetic measurements laboratories. Hence, the method can be a valid substitute of other not always available techniques for weakly magnetic materials characterization, such as the VSM and the SQUID magnetometry. Moreover, in contrast with these two techniques, the SSM does not require sophisticated calibration techniques of the apparatus and the use of a cryogen to work. Another advantage is the possibility to test material samples of arbitrary shape within the magnet's aperture limitations. A possible drawback could be the range of possible test fields that depend on the available magnets in the measurement laboratory.

A cryogenic version of this system having a cold sample in a warm bore is currently under development to test the permeability of weakly magnetic materials at temperatures compatible with applications, such as aerospace or superconducting magnets for particle accelerators (1.9 and 4.2 K).

Acknowledgment

The authors thank the European Organization for Nuclear Research (CERN) colleagues S. Sorti for the precious help with the electromagnetic modeling aspects, A. T. Perez Fontenla for the help with the assessment of the EDM machining effects, G. Deferne, M. Liebsch, and A. Beaumont and N. Bruti for the technical support. This work was carried out at the Magnetic Measurement Section, CERN.

References

[1] A. Parrella, "Magnetic material characterization and magnet axis displacement measurement for particle accelerators," Ph.D. dissertation, Dept. Elect. Eng. Inf. Technol., Univ. Naples Federico II, Univ. Lisbon IST, Naples, Italy, 2018.

[2] G. S. Brady, H. R. Clauser, and J. A. Vaccari, *Materials Handbook*, 15th ed. New York, NY, USA: McGraw-Hill, 2002.

[3] A. Mehjabeen, T. Song, W. Xu, H. P. Tang, and M. Qian, "Zirconium alloys for orthopaedic and dental applications," *Adv. Eng. Mater.*, vol. 20, no. 9, Sep. 2018, Art. no. 1800207.

[4] *Standard Test Methods for Permeability of Weakly Magnetic Materials*, Standard A342/A342M-14, ASTM, 2014.

[5] P. Arpaia, A. Liccardo, M. Buzio, and A. Parrella, "On the use of fluxmetric methods for characterizing feebly magnetic materials," in *Proc. IEEE Int. Instrum. Meas. Technol. Conf. (IMTC)*, May 2017, pp. 1–6.

[6] Severn Engineering. *Low MU Permeability Indicator*. Accessed: Jan. 2020. [Online]. Available: https://severnengineering.com/lomu/

[7] Institut Dr. Foerster GmbH. (2019). *Foerster Magnetoscop 1.070 Datasheet*. [Online]. Available: http://www.foerstergroup.com/en/usa/products/magnetoscop-1070/

[8] S. Foner, "Vibrating sample magnetometer," *Rev. Sci. Instrum.*, vol. 27, no. 7, p. 548, 1956, doi: 10.1063/1.1715636.

[9] R. L. Fagaly, "Superconducting quantum interference device instruments and applications," *Rev. Sci. Instrum.*, vol. 77, no. 10, Oct. 2006, Art. no. 101101.

[10] *International Comparison of Measurements of the Magnetic Moment Using Vibrating Sample Magnetometers (VSM) and Superconducting Quantum Interference Device (SQUID) Magnetometers*, Standard TR 62797:2013, IEC, 2013.

[11] P. Flanders, "An alternating-gradient magnetometer," *J. Appl. Phys.*, vol. 63, no. 8, pp. 3940–3945, 1988.

[12] C. D. Graham and B. E. Lorenz, "Delta ferrite is ubiquitous in type 304 stainless steel: Consequences for magnetic characterization," *J. Magn. Magn. Mater.*, vol. 458, pp. 15–18, Jul. 2018.

[13] A. Borna, T. R. Carter, P. DeRego, C. D. James, and P. D. Schwindt, "Magnetic source imaging using a pulsed optically pumped magnetometer array," *IEEE Trans. Instrum. Meas.*, vol. 68, no. 2, pp. 493–501, Feb. 2019.

[14] J. E. Green, D. A. Stone, M. P. Foster, and A. Tennant, "Spatially resolved measurements of magnetic fields applied to current distribution problems in batteries," *IEEE Trans. Instrum. Meas.*, vol. 64, no. 4, pp. 951–958, Apr. 2015.

[15] L. Fan *et al.*, "A fast linear algorithm for magnetic dipole localization using total magnetic field gradient," *IEEE Sensors J.*, vol. 18, no. 3, pp. 1032–1038, Feb. 2018.

[16] D. Cichon, R. Psiuk, H. Brauer, and H. Töpfer, "A Hall-sensor-based localization method with six degrees of freedom using unscented Kalman filter," *IEEE Sensors J.*, vol. 19, no. 7, pp. 2509–2516, Apr. 2019.

[17] T. Schlegl, M. Neumayer, S. Mühlbacher-Karrer, and H. Zangl, "A pretouch sensing system for a robot grasper using magnetic and capacitive sensors," *IEEE Trans. Instrum. Meas.*, vol. 62, no. 5, pp. 1299–1307, May 2013.

[18] M. Yin, X. Liu, Y. Liu, and X. Chen, "Medical image fusion with parameter-adaptive pulse coupled neural network in nonsubsampled shearlet transform domain," *IEEE Trans. Instrum. Meas.*, vol. 68, no. 1, pp. 49–64, Jan. 2019.

[19] A. A.-E. Abdallh and L. Dupre, "A unified electromagnetic inverse problem algorithm for the identification of the magnetic material characteristics of electromagnetic devices including uncertainty analysis: A review and application," *IEEE Trans. Magn.*, vol. 51, no. 1, pp. 1–10, Jan. 2015.

[20] G. Schubert and P. Harrison, "Magnetic induction measurements and identification of the permeability of magneto-rheological elastomers using finite element simulations," *J. Magn. Magn. Mater.*, vol. 404, pp. 205–214, Apr. 2016.

[21] J. Dong, G. Zhang, Y. Geng, and J. Wang, "Current distribution reconstruction in low-voltage circuit breakers based on magnetic inverse problem solution considering ferromagnetic splitters," *IEEE Trans. Magn.*, vol. 54, no. 10, pp. 1–9, Oct. 2018.

[22] P. Arpaia, A. Liccardo, A. Parrella, P. Ramos, and M. Buzio, "Inverse problem-based magnetic characterization of weekly magnetic alloys," in *Proc. IPAC*, 2017, pp. 4722–4725.

[23] O. Bíró, C. Paul, and K. Preis, "The use of a reduced vector potential A_r formulation for the calculation of iron induced field errors," CERN, Meyrin, Switzerland, Tech. Rep. OPEN-2000-150, 1999.

[24] K. Levenberg, "A method for the solution of certain non-linear problems in least squares," *Quart. Appl. Math.*, vol. 2, no. 2, pp. 164–168, 1944.

[25] D. W. Marquardt, "An algorithm for least-squares estimation of nonlinear parameters," *J. Soc. Ind. Appl. Math.*, vol. 11, no. 2, pp. 431–441, Jun. 1963.

[26] Metrolab Technology SA. (Nov. 2019). *PT2025 NMR Precision Teslameter Specifications*. [Online]. Available: https://www.metrolab.com/products/pt2025/

[27] Physik Instrumente. (Sep. 2020). *M-511, M-521, M-531 High-Precision Linear Stage Datasheet*. [Online]. Available: https://static.physikinstrumente.com/fileadmin/user_upload/physik_instrumente/files/datasheets/M-511-Datasheet.pdf

[28] Tektronix Inc. (Sep. 2020). *Keithley 2700, 2701, and 2750 Multimeter/Data Acquisition/Switch Systems*. [Online]. Available: https://www.tek.com/keithley-switching-and-data-acquisition-systems/keithley-2700-multimeter-data-acquisition-switch-sys

[29] Leica Geosystems. (Sep. 2020). *Leica Absolute Tracker AT930*. [Online]. Available: https://www.hexagonmi.com/products/laser-tracker-systems/leica-absolute-tracker-at930

[30] F. R. Fickett and R. P. Reed, *Advances in Cryogenic Engineering Materials*, vol. 38. Berlin, Germany: Springer, 1991.

[31] *Evaluation of Measurement Data, Guide to the Expression of Uncertainty in Measurement*, BIPM, IEC, IFCC, ILAC, ISO, IUPAC, IUPAP, OIML, Joint Committee Guides Metrol., Sèvres, France, 2008.

[32] *Evaluation of Measurement Data, Supplement 1 to the GUM: Propagation of Distributions Using a Monte Carlo Method*, Joint Committee Guides Metrol., Sèvres, France, 2008.

Pasquale Arpaia (Senior Member, IEEE) received the master's and Ph.D. degrees in electrical engineering from the University of Naples Federico II, Naples, Italy, in 1987 and 1992, respectively.

He was a Professor with the University of Sannio, Benevento, Italy, and an Associate at the Institutes of Engines and Biomedical Engineering of CNR. He is an Associate at the INFN Section of Naples. He is currently a Full Professor of instrumentation and measurements with the University of Naples Federico II. He is also the Head of the Instrumentation and Measurement for Particle Accelerators Laboratory (IMPALab) and the Augmented Reality for Health Monitoring Laboratory (ARHeMlab). He is also a Team Manager at European Organization for Nuclear Research (CERN), Geneva, Switzerland, the Deputy Chairman of the Interdepartmental Center for Research on Management and Innovation of Health (CIRMIS), the Head of the Hi-Tech Academic FabLab Unina DIETI, and the Chairman of the Stage Project of the University Federico II. In last years, he was scientific responsible of more than 30 awarded research projects in cooperation with industry, with related patents and international licenses, and funded four academic spin-off companies. His main research interests include instrumentation and measurement for magnets, advanced materials, beam, superconductors, power converters, and cryogenics of particle accelerators, biomedical instrumentation, augmented reality, brain–computer interfaces, evolutionary diagnostics, distributed measurement systems, and analog-to-digital converter (ADC) modeling and testing. In these fields, he published three books, several book chapters, and about 300 scientific papers in journals and national and international conference proceedings.

Dr. Arpaia has served as an organizing and scientific committee member in several IEEE and IMEKO conferences. His Ph.D. students were awarded in 2006, 2010, and 2020 at IEEE I2MTC, as well as in 2016 and 2012 at IMEKO TC-10 and in 2018 at World Conferences. He is an Associate Editor of the *Journal of Instrumentation* (Institute of Physics), *Computer Standards & Interfaces* (Elsevier journal), *Instruments* (MDPI). He was an Associate Editor of the IEEE TRANSACTIONS ON ELECTRONICS PACKAGING AND MANUFACTURING. He was an Editor at Momentum Press of the Book Collection *Emerging Technologies in Measurements, Instrumentation, and Sensors*. He acted as a scientific evaluator in several international research call panels. He is a plenary speaker in several scientific conferences.

Marco Buzio received the M.Sc. degree in aerospace engineering from the Polytechnic of Milan, Milan, Italy, in 1992 and the Ph.D. degree in computational mechanics from Imperial College London, London, U.K, in 1998.

He has worked on the electromechanical modeling of fusion devices at the JET Tokamak, Abingdon, U.K. He is currently a Senior Engineer in the field of magnetic measurements for particle accelerators at the European Organization for Nuclear Research (CERN), Geneva, Switzerland. His main research interests include measurement techniques, modeling and control of hysteretic and fast-pulsed magnets, the design and metrological characterization of induction-coil and magnetic-resonance-based sensors, inverse measurement techniques for current distribution, and magnetic material properties.

Dr. Buzio is on the Organizing Board of the International Magnetic Measurement Workshop.

Alessandro Parrella graduated in electronic engineering for telecommunication from the University of Sannio, Benevento, Italy, in 2014. He received the double Ph.D. degrees in electrical engineering and computer science from the University of Naples Federico II, Naples, Itay, and the Instituto Superior Técnico, University of Lisbon, Lisbon, Portugal, in 2018.

He is currently a Senior Fellow Researcher with the Superconducting Magnets and Cryostats Group, European Organization for Nuclear Research (CERN), Geneva, Switzerland. His research activity deals with real-time magnetic measurement systems. He has also worked extensively on the characterization of magnetic materials for particle accelerator components.

Mariano Pentella (Student Member, IEEE) received the M.Sc. degree in electrical engineering from the University of Naples Federico II, Naples, Italy, in 2018. He is currently pursuing the Ph.D. degree in metrology with the Polytechnic of Turin, Turin, Italy.

He carries out his research activity in the framework of the collaboration between the Magnetic Measurement Section at the European Organization for Nuclear Research (CERN), Geneva, Switzerland, and the Department of Applied Science and Technology at the Polytechnic of Turin. His current research interests include the development of novel measurement methods to characterize magnetic materials and modeling techniques to predict the hysteretic behavior in ferromagnetic materials.

Pedro M. Ramos (Senior Member, IEEE) was born in Lisbon, Portugal, in 1972. He received the Diploma, master's, and Ph.D. degrees in electrical and computer engineering from the Instituto Superior Técnico, Technical University of Lisbon (now University of Lisbon—UL), Lisbon, Portugal, in 1995, 1997, and 2001, respectively.

He is currently an Associate Professor with habilitation at the Instituto Superior Técnico, UL, and a Senior Researcher with the Instrumentation and Measurement Research Group, Instituto de Telecomunicações. His current research interests include impedance measurements, impedance spectroscopy, sine-tting algorithms, automatic measurement systems, power-quality monitoring/measurements, and nondestructive electronic measurement systems.

Dr. Ramos has been a member of IMEKO TC4-Measurement of Electrical Quantities since 2006. He was the Scientific Secretary of IMEKO T4 from 2012 to 2014 and the Vice-Chair of IMEKO TC4 from 2015 to 2018.